Stability Enhancement of Multi-Infeed HVDC Systems Using Grid-Forming Control under Weak Grid Conditions

Muhammad Fawad[1,2], Akansha Garg[2], Mohamed Galeela[2,3], Chuanyue Li[1], Jun Liang[1]

[1]*School of Engineering, Cardiff University, Cardiff, GB*

[2]*Energy Networks, TNEI Services Ltd, Manchester, GB*

[3]*Electrical Power Engineering Department, Cairo University, Egypt*

***Abstract*—This paper addresses critical stability challenges in multi-infeed voltage-source converter high-voltage direct current (VSC–HVDC) systems integrating offshore wind under weak-grid conditions. Through rigorous analytical modeling and electromagnetic transient (EMT) validation, we demonstrate that grid-following (GFL) converters exhibit fundamental instability during short-circuit ratio (SCR) reduction, with critical conjugate eigenvalue pairs migrating to the right half-plane. In contrast, grid-forming (GFM) converters maintain robust stability through inherent voltage-source behavior and droop control mechanisms. Hybrid GFL-GFM multi-infeed system reveals that GFM integration fundamentally transforms system dynamics, shifting critical poles from unstable right-half-plane positions to well-damped left-half-plane locations. This stabilization capability is critically governed by electrical distance, with GFM providing effective support across moderate separation distances under SCR$\in[2,3]$, while closer proximity becomes essential under severe grid weakness (SCR≈1) to maintain adequate stability margins. These findings establish GFM control as indispensable for offshore HVDC resilience and provide fundamental insights for converter placement strategies and system planning under N-1 contingency scenarios.**

***Index Terms*—HVDC systems, offshore wind integration, GFL, GFM, weak grid stability, SCR, multi-infeed HVDC**

I. Introduction

The global expansion of offshore wind generation, coupled with conventional synchronous generator retirements, is accelerating voltage-source converter high-voltage direct current (VSC-HVDC) adoption for bulk power transmission and asynchronous interconnection [1], [2]. While VSC-HVDC systems offer enhanced controllability, their dynamic performance under weak-grid conditions presents fundamental stability challenges. The short-circuit ratio (SCR) serves as the critical grid-strength indicator: diminishing SCR reduces electrical stiffness and exacerbates adverse converter-grid interactions, pushing conventional control architectures to operational limits [3], [4].

The prevailing grid-following (GFL) paradigm employs phase-locked loop (PLL) synchronization from measured terminal voltages. Under low SCR conditions, PLL dynamics interact with inner current and outer power control loops, introducing negative damping and precipitating oscillatory instabilities that compromise system security [3], [5]. Conversely, grid-forming (GFM) converters establish voltage and frequency, typically through mechanisms P–ω droop mechanisms, functioning as voltage sources behind impedance. This architecture inherently enhances angle stability, provides frequency support, and demonstrates superior robustness to grid impedance variations, making it particularly suited for weak-grid, high-renewable systems [6].

Modern offshore integration increasingly employs multi-infeed HVDC topologies where multiple converters share a common coupling point (PCC) through parallel AC corridors [7]. These configurations, often resulting from phased development, introduce significant dynamic cross-coupling. Contingencies such as AC corridor loss instantaneously reduce effective SCR, altering impedance characteristics and amplifying control interactions across the PCC.

This paper analyzes multi-infeed HVDC stability under SCR reduction due to AC line outage. Small-signal models of GFL and GFM converters are validated with EMT simulations, and eigenvalue migration in hybrid GFL–GFM operation is examined, showing critical modes shifting from RHP to LHP. The impact of electrical distance and GFM support on adjacent GFL terminals is quantified, providing guidance for control coordination and offshore grid planning.

II. Multi-Infeed HVDC System Description

The studied network (Fig. 1) consists of two parallel ±320 kV VSC–HVDC links with cable lengths of 150 km (Infeed I) and 100 km (Infeed II), transmitting offshore wind power to a common onshore PCC. Key components relevant to the stability analysis are described here, while detailed parameters are listed in Table I.

A. System Configuration and HVDC Links

Offshore converters (Stations II and IV) connect aggregated wind farms via passive LC filters, with pre-insertion resistors for controlled energization. Onshore, Station I is directly connected to the PCC, whereas Station III is linked through series impedance $(R_{\mathrm{S-III}}, L_{\mathrm{S-III}})$ to create electrical separation and enable multi-infeed interaction analysis. Offshore converters regulate DC voltage, while onshore units control active power, forming a structured framework for stability assessment under varying grid strength.

979-8-3315-8138-1

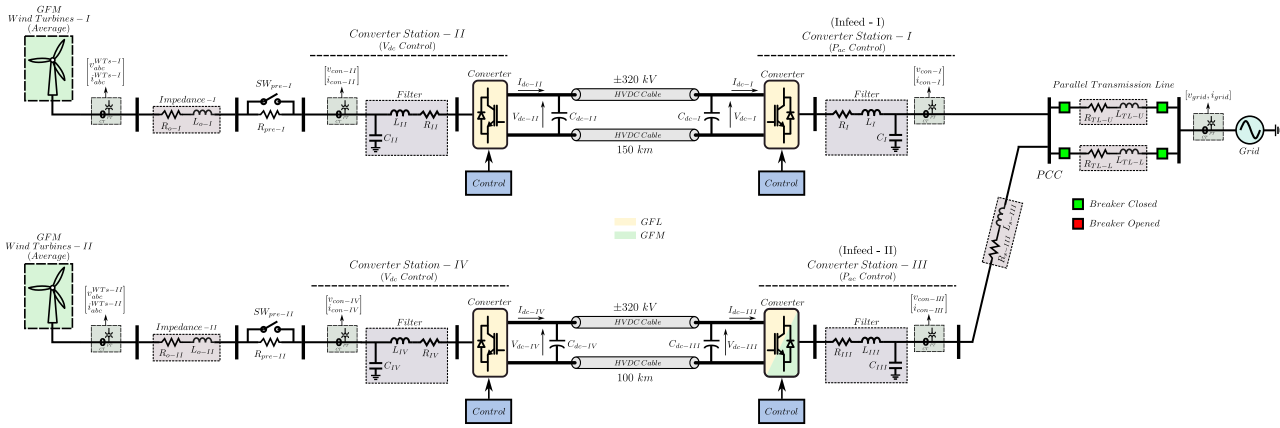

Fig. 1. Two-infeed VSC–HVDC system with asymmetric onshore connections and parallel grid ties.

TABLE I
COMPREHENSIVE SYSTEM PARAMETERS FOR MULTI-INFEED VSC–HVDC CONFIGURATION

Parameter	Symbol	Value
AC grid voltage (LL, rms)	V_{AC}	400 kV
DC pole voltage	V_{DC}	±320 kV
Upper HVDC cable length	$L_{c,\mathrm{up}}$	150 km
Lower HVDC cable length	$L_{c,\mathrm{lo}}$	100 km
Grid upper/lower line resistance	$R_{\mathrm{TL\text{-}U}} = R_{\mathrm{TL\text{-}L}}$	*7.96* Ω
Grid upper/lower line inductance	$L_{\mathrm{TL\text{-}U}} = L_{\mathrm{TL\text{-}L}}$	*0.2533* H
Station III tie impedance to PCC	$R_{\mathrm{S-III}} + jXL_{\mathrm{S-III}}$	*2.5+j7.85* Ω
DC capacitor (Station I / II)	$C_{\mathrm{dc-I}} = C_{\mathrm{dc-II}}$	*500* uF
DC capacitor (Station III / IV)	$C_{\mathrm{dc-III}} = C_{\mathrm{dc-IV}}$	*350* uF
Pre-insertion resistor	$R_{\mathrm{pre-I}} = R_{\mathrm{pre-II}}$	*25* Ω
Offshore line resistance	$R_{\mathrm{o-I}} = R_{\mathrm{o-II}}$	*5.59* Ω
Offshore line inductance	$L_{\mathrm{o-I}} = L_{\mathrm{o-II}}$	*0.05* H
PLL PI Proportional gains	$k_{p\theta}$	*890*
PLL PI Integral gains	$k_{i\theta}$	*400000*
Outer Power PI gains (GFL)	k_{pp} / k_{ip}	*0.01 / 100*
Inner Current PI gains (GFL)	k_{pi} / k_{ii}	*0.5 / 500*
Outer PI gains (GFM)	k_{pv} / k_{iv}	*2 / 1000*
Inner PI gains (GFM)	k_{pi} / k_{ii}	*2 / 3500*
GFM active-power droop	k_{p-I}	*3* %

B. AC Grid Strength and Contingency Scenario

The onshore grid is modeled by two parallel R–L corridors. An N–1 outage at $t = 3$ s disconnects one line, reducing the SCR from ≈4 to ≈2.

C. Converter Control Strategies

This study assesses two onshore control strategies under weak-grid conditions: (i) GFL control with PLL-based synchronization and cascaded power-current loops, and (ii) GFM control based on P–ω droop to set voltage and frequency while tracking active power. Both an all-GFL and a hybrid GFL–GFM configuration are analyzed. Corresponding small-signal models and eigenvalue analysis (Section III) provide the basis for multi-infeed stability evaluation.

III. MODELLING AND STABILITY ASSESSMENT OF GFL AND GFM CONVERTERS

This section presents analytical models of onshore converters to capture dominant active-power synchronization dynamics under variable grid strength for both GFL and GFM controls, supporting eigenvalue analysis. Model accuracy is verified against EMT simulations of the single-infeed system (Fig. 2). The PCC network is represented by an equivalent Thévenin impedance (R_g, L_g), where symmetric parameters yield $R_g = R_{\mathrm{TL-U}}/2$ and $L_g = L_{\mathrm{TL-U}}/2$, allowing direct emulation of SCR variation via L_g.

A. GFL Converter Model

The onshore GFL converter is modeled using the control structure shown in Fig. 3. The converter dynamics are captured by the state-space representation [3], [8]:

$$\frac{d}{dt}\begin{bmatrix} i_d \\ i_q \end{bmatrix} = -\begin{bmatrix} \frac{R_{\mathrm{tot}}}{L_{\mathrm{tot}}} & 0 \\ 0 & \frac{R_{\mathrm{tot}}}{L_{\mathrm{tot}}} \end{bmatrix}\begin{bmatrix} i_d \\ i_q \end{bmatrix} + \begin{bmatrix} \frac{1}{L_{\mathrm{tot}}} & 0 \\ 0 & \frac{1}{L_{\mathrm{tot}}} \end{bmatrix}(\mathbf{v}_{dq} - \mathbf{v}_{\mathrm{PCC}}), \tag{1}$$

with $R_{\mathrm{tot}} = R_1 + R_g$ and $L_{\mathrm{tot}} = L_1 + L_g$. The inner current controller is

$$\mathbf{u}_{dq}(s) = \left(k_{pi} + \frac{k_{ii}}{s}\right)(\mathbf{i}_{dq}^{\mathrm{ref}} - \mathbf{i}_{dq}), \tag{2}$$

yielding the closed-loop transfer matrix:

$$\Delta i_d(s) = G_i(s)\,\Delta i_d^*(s) \tag{3}$$

$$G_{inner}(s) = \frac{k_{pi}s + k_{ii}}{L_{\mathrm{tot}}s^2 + (R_{\mathrm{tot}} + k_{pi})\,s + k_{ii}}. \tag{4}$$

Around $v_{q0} \approx 0$ and $i_{q0} \approx 0$, $\Delta P \approx \frac{3}{2}V_d\,\Delta i_d$, and the outer active-power PI is

$$\Delta i_d^*(s) = \left(k_{pp} + \frac{k_{ip}}{s}\right)\left(\Delta P_{conv-I}^*(s) - \Delta P_{conv-I}(s)\right). \tag{5}$$

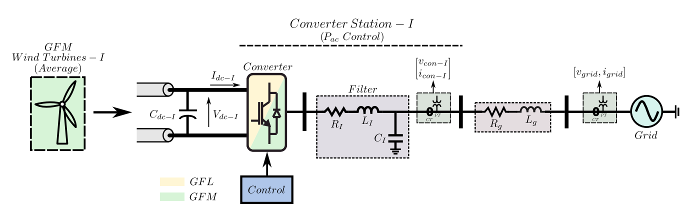

Fig. 2. Single-infeed test configuration for GFL/GFM controller validation under variable SCR.

979-8-3315-8138-1

The synchronizing-loop (PLL) small-signal model introduces the angle state $\Delta\theta$ and integrator state $\Delta\xi_\theta$:

$$\Delta\dot{\theta} = \Delta\omega, \quad \Delta\omega = k_{p\theta}\Delta v_q^\theta + k_{i\theta}\Delta\xi_\theta, \quad \Delta\dot{\xi}_\theta = \Delta v_q^\theta, \quad (6)$$

with the linearized frame coupling at $(v_{q0} \approx 0,\ v_{d0} = V_d)$:

$$\Delta v_q^\theta \approx \Delta v_q - V_d\,\Delta\theta. \quad (7)$$

Eliminating $\Delta\omega$ and $\Delta\xi_\theta$ gives

$$P(s) = \frac{\Delta\theta(s)}{\Delta v_q(s)} = \frac{k_{p\theta}s + k_{i\theta}}{D_\theta(s)}, \quad (8)$$

$$D_\theta(s) = s^2 + V_d k_{p\theta} s + V_d k_{i\theta}. \quad (9)$$

Under weak-grid conditions, the q-axis PCC voltage perturbation is coupled to injected d-axis current through the inductive drop, $\Delta v_q(s) \approx -\omega_0 L_g\,\Delta i_d(s)$, and the corresponding first-order power perturbation in the rotating frame can be expressed as $\Delta P \approx \frac{3}{2}V_d\,(\Delta i_d + I_{d0}\Delta\theta)$. Substitution yields

$$\Delta P_{conv-I}(s) = \left(\frac{3}{2}V_d\,G_i(s)\right)[1 - \omega_0 L_g I_{d0} P(s)\Delta i_d^*(s). \quad (10)$$

Hence the loop gain is

$$L(s) = \left(\frac{3}{2}V_d\,G_i(s)\right)\left(k_{pp} + \frac{k_{ip}}{s}\right)[1 - \omega_0 L_g I_{d0} P(s)]. \quad (11)$$

and the closed-loop transfer function is

$$\frac{P_{conv-I}(s)}{P^*_{conv-I}(s)} = \frac{L(s)}{1 + L(s)}. \quad (12)$$

When the synchronizing-loop bandwidth is high relative to the outer power loop, $D_\theta(s) \gg \omega_0 L_g I_{d0}(k_{p\theta}s + k_{i\theta})$ over the frequency range of interest, so the bracketed term in (11) approaches unity and (12) reduces to

$$\frac{P_{conv-I}(s)}{P^*_{conv-I}(s)} = \frac{N(s)}{D(s)}, \quad (13)$$

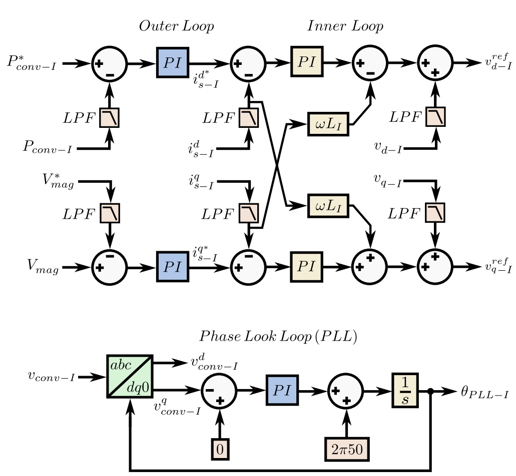

Fig. 3. GFL converter control with PLL and cascaded power and current controller.

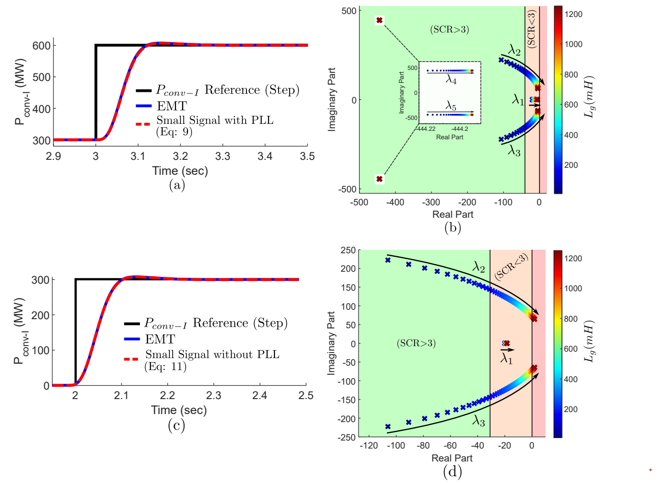

Fig. 4. GFL model validation. (a) EMT vs. full model (300–600 MW step). (b) Eigenvalues: fast PLL poles vs. dominant power modes. (c) EMT vs. reduced model (13) (0–300 MW step). (d) Eigenvalue migration with L_g showing weak-grid instability.

with

$$N(s) = \frac{3}{2}V_d\left[k_{pp}k_{pi}s^2 + (k_{pp}k_{ii} + k_{ip}k_{pi})\,s + k_{ip}k_{ii}\right],$$
$$D(s) = L_{\text{tot}}s^3 + a_2 s^2 + a_1 s + a_0,$$

where

$$a_2 = R_{\text{tot}} + k_{pi} + \tfrac{3}{2}V_d k_{pp}k_{pi},$$
$$a_1 = k_{ii} + \tfrac{3}{2}V_d(k_{pp}k_{ii} + k_{ip}k_{pi}),$$
$$a_0 = \tfrac{3}{2}V_d k_{ip}k_{ii}.$$

The GFL small-signal model includes PLL dynamics ($\Delta\theta$, $\Delta\xi_\theta$) and frame transformation $\Delta v_q^\theta \approx \Delta v_q - V_d\Delta\theta$. Under weak-grid conditions, $\Delta P \approx \frac{3}{2}V_d(\Delta i_d + I_{d0}\Delta\theta)$ couples the PLL to the power loop. With PLL bandwidth much higher than the power loop, time-scale separation allows ΔP to use a coupling factor ≈ 1, enabling a reduced-order model that removes fast PLL poles while retaining dominant active-power modes for eigenvalue analysis.

Figure 4 validates the full and reduced models. (a) EMT response to a 300–600 MW step closely follows the full linear model (1)–(12). (b) PLL poles lie deep in the LHP, confirming faster dynamics than the dominant power-synchronization modes. (c) The reduced transfer function (13) accurately reproduces the 0–300 MW EMT response. (d) Increasing L_g shifts the critical mode toward the RHP, explaining damping reduction and oscillatory instability under weak-grid conditions.

B. GFM Converter Modeling

The onshore GFM control (Fig. 5) uses P–ω droop for active-power synchronization. Small-signal analysis assumes high-bandwidth inner loops with $v_{PCC} \approx 1$ pu and $q \approx 0$, isolating the dominant power–frequency dynamics. Inner loop poles exist at high frequency in the LHP but do not affect the main droop eigenvalue governing weak-grid stability.

979-8-3315-8138-1

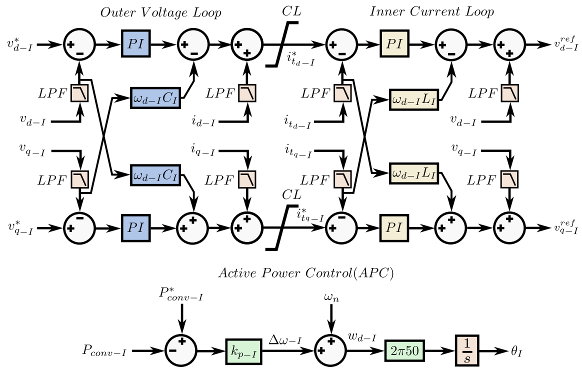

Fig. 5. GFM converter control with $P-\omega$ droop and cascaded voltage and current controllers.

The GFM converter is modeled as a controllable internal voltage behind a coupling reactance, following standard droop-based formulations [9], [10]. Steady-state active power is then determined by the power–angle relation across this reactance.

$$P_{conv-I} \;=\; \frac{E_I\, v_{d-I}}{X_{eq-I}}\, \sin\delta_I, \tag{14}$$

where $\delta_I \triangleq \theta_I - \theta_g$ is the converter–grid angle, E_I is the internal emf magnitude set by the voltage controller, v_{d-I} is the PCC d-axis voltage (pu), and $X_{eq-I} \approx \omega_0(L_1+L_g)$ collects the filter and grid at ω_0. Linearizing (14) at $\delta_I^0 \simeq 0$ gives

$$\Delta P_{conv-I} \;\approx\; K_{s-I}\,\Delta\delta_I, \qquad K_{s-I} \;\triangleq\; \frac{E_I\, v_{d-I}}{X_{eq-I}}, \tag{15}$$

with K_{s-I} the synchronizing (power) coefficient. The P–ω droop and angle integrator are

$$\Delta\omega_I \;=\; k_{p-I}\big(\Delta P^{\star}_{conv-I} - \Delta P_{conv-I}\big), s\,\Delta\delta_I \;=\; \Delta\omega_I, \tag{16}$$

with k_{p-I} the droop gaig. Eliminating $\Delta\delta_I$ and $\Delta\omega_I$ gives the first-order transfer function

$$\frac{\Delta P_{conv-I}(s)}{\Delta P^{\star}_{conv-I}(s)} \;=\; \frac{k_{p-I}K_{s-I}}{s + k_{p-I}K_{s-I}}, \tag{17}$$

with time constant $\tau = 1/(k_{p-I}K_{s-I})$. Whose single eigenvalue is $\lambda_1 = -k_{p-I}K_{s-I} < 0$.

A 300 MW reference step shows that model (17) closely matches the EMT response, capturing both transients and steady state (Fig. 6(a)). Eigenvalue analysis under weaker grids (Fig. 6(b)) shows that increasing X_{eq} lowers synchronization stiffness K_s, moving the dominant mode λ_1 toward the origin while remaining stable. Unlike GFL, the GFM converter stays stable, with slower transient dynamics as grid strength decreases.

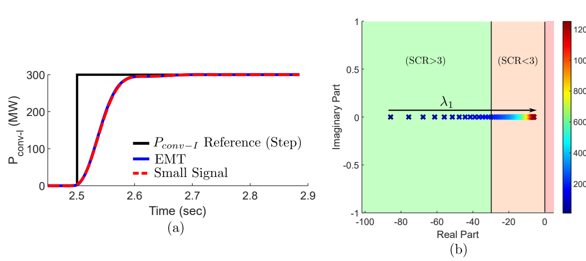

Fig. 6. GFM model validation: (a) Step response comparison; (b) Eigenvalue sensitivity to grid impedance.

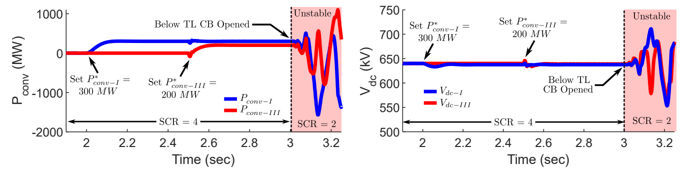

Fig. 7. Multi-Infeed GFLs: Converters I and III Active power and Corresponding DC-link voltage.

IV. Multi-Infeed HVDC Dynamics under SCR Variation

This section examines the two-infeed HVDC response to a severe grid event: at $t=3$ s, the lower AC corridor outage reduces SCR from ≈ 4 to ≈ 2, increasing PCC Thévenin reactance and intensifying converter coupling, thereby testing synchronization stability under weak-grid conditions.

A. Multi-Infeed GFL Instability During Line Contingency

The $t = 3$ s contingency reduces SCR from 4 to 2, raising PCC Thévenin reactance and weakening damping of the dominant modes $\{\lambda_2, \lambda_3\}$, determined by the outer active-power PI and inner current-control interaction with the weak grid and multi-infeed coupling. This defines a critical boundary between stability and oscillatory instability.

The instability causes sustained $P_{\text{conv}-\text{I}}$ and $P_{\text{conv}-\text{III}}$ oscillations and large V_{dc} variations. Eigenvalue analysis confirms the dominant mode crosses the imaginary axis under weak-grid conditions (Fig. 7).

B. Hybrid GFL-GFM Stabilization During Line Contingency

The hybrid system with Converter I (GFL, 300 MW) and Converter III (GFM, 200 MW) remains stable after the $t = 3$ s corridor outage (SCR $4 \to 2$). Stability is supported by the GFM converter, whose voltage-source behavior and P–ω droop maintain synchronism through internal angle adjustment (Fig. 8).

The GFM converter provides inherent synchronizing damping, counteracting GFL negative damping. DC voltages remain stable with minimal deviations, and the hybrid setup prevents the oscillatory instability seen in all-GFL operation,

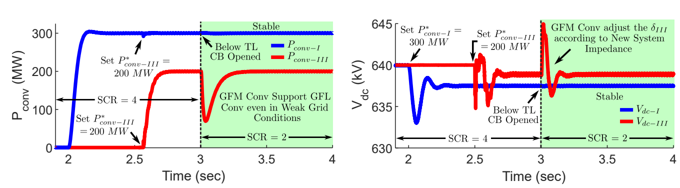

Fig. 8. Hybrid GFL-GFM Infeed: Converters I and III Active power and Corresponding DC-link voltage.

979-8-3315-8138-1

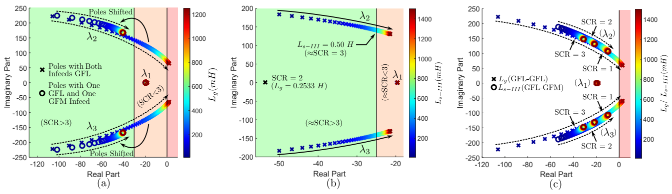

Fig. 9. Eigenvalue analysis: (a) GFL-GFL vs. GFL-GFM pole migration; (b) Critical L_{s-III} value at SCR=2; (c) Stability boundaries vs. L_{s-III} at different SCR.

highlighting GFM's role in maintaining stability under severe grid weakening.

C. Eigenvalue Analysis of Multi-Infeed Stability

Eigenvalue analysis clarifies multi-infeed stability under SCR reduction. As L_g increases, the all-GFL case ($\times$) shows conjugate modes moving toward the RHP, indicating negative damping, whereas the hybrid GFL–GFM case ($\circ$) shifts modes deeper into the LHP due to GFM synchronization stiffness and voltage-source behavior (Fig. 9(a)).

Figure 9(b) shows the impact of electrical distance $L_{S\text{–}III}$ on GFM support under SCR ≈ 2. Increasing $L_{S\text{–}III}$ weakens coupling to the PCC, reducing synchronizing stiffness and damping to the adjacent GFL terminal, reflected by rightward migration of dominant modes. Beyond $L_{S\text{–}III}\approx 0.5$ H, damping degrades markedly, indicating the limit of effective remote GFM support. Nevertheless, stability remains superior to the all-GFL case due to retained voltage-source characteristics.

Figure 9(c) presents a stability map obtained by sweeping L_g (SCR variation) and $L_{S\text{–}III}$ (electrical distance). For each $(L_g, L_{S\text{–}III})$, system eigenvalues are computed. Under moderate grids (SCR $\approx$ 3), the hybrid GFL–GFM system remains stable even with large separation. As SCR decreases, increasing $L_{S\text{–}III}$ reduces damping and shifts dominant modes rightward, indicating that effective GFM support requires closer proximity. In contrast, the all-GFL case becomes oscillatory unstable under severe grid weakening.

V. Conclusion

This paper quantified the small-signal stability of GFL and GFM VSC–HVDC terminals under varying grid strength, validated against EMT. For GFL control, SCR reduction (increased PCC Thevenin inductance) lowers damping of the dominant active-power synchronization mode and can drive the critical conjugate pair into the right-half plane. In contrast, the GFM droop-synchronization mode remains in the left-half plane over the same weakening range, exhibiting reduced bandwidth but no oscillatory instability.

The analysis was extended to a two-infeed HVDC system with an N–1 AC corridor outage reducing SCR from ~ 4 to ~ 2. In the all-GFL case, stronger coupling yields sustained active-power oscillations and large DC-link voltage excursions, consistent with eigenvalue migration. With one terminal in GFM mode, the coupled eigenstructure is reshaped, dominant modes shift to well-damped left-half-plane locations, and stable EMT recovery is restored.

Figure 9(c) shows a stability map obtained by sweeping L_g (SCR variation) and $L_{S\text{–}III}$ (electrical distance). For each $(L_g, L_{S\text{–}III})$, small-signal eigenvalues are evaluated. With moderate grids (SCR $\approx$ 3), the hybrid GFL–GFM system remains stable even at large separation. As SCR decreases, increasing $L_{S\text{–}III}$ weakens damping and shifts dominant modes toward the RHP, indicating that effective GFM support becomes distance-limited. By contrast, the all-GFL configuration enters oscillatory instability under severe grid weakening.

VI. Acknowledgment

This work was supported by the ADOreD (Accelerating the Deployment of Offshore Wind using DC Technology) project and by UKRI through the Strategic Advancement on Offshore Multi-Terminal DC Networks (MTDC) for Enhanced System Services project.

The authors declare that all research concepts, analyses, and conclusions are their original work. ChatGPT was used only for language editing and grammar refinement; no technical content, data analysis, or results were generated by AI tools.

References

[1] A. Korompili, Q. Wu, and H. Zhao, "Review of VSC HVDC connection for offshore wind power integration," *Renewable & Sustainable Energy Reviews*, vol. 59, pp. 1405–1414, 2016. [Online]. Available: https://backend.orbit.dtu.dk/ws/portalfiles/portal/119791019/Review_of_VSC_HVDC_Connection_for_Offshore_Wind.pdf

[2] L. F. N. Lourenço, A. Louni, G. Damm, M. Netto, M. Drissi-Habti, S. Grillo, A. J. S. Filho, and L. Meegahapola, "A review on multi-terminal high voltage direct current networks for wind power integration," *Energies*, vol. 15, no. 23, p. 9016, 2022. [Online]. Available: https://www.mdpi.com/1996-1073/15/23/9016

[3] A. Nicolini, H. Pinheiro, F. Carnielutti, and J. Massing, "Pll parameters tuning guidelines to increase stability margins in multiple three-phase converters connected to weak grids," *IET Renewable Power Generation*, 2020. [Online]. Available: https://ietresearch.onlinelibrary.wiley.com/doi/epdf/10.1049/iet-rpg.2020.0028

[4] C. Li, S. Wang, and J. Liang, "Tuning method of a grid-following converter for the extremely-weak-grid connection," *IEEE Transactions on Power Systems*, vol. 37, no. 4, pp. 3169–3172, 2022.

[5] Y. Zhou, Z. Deng, S. Chen, Y. Qiu, T. Zang, and B. Zhou, "A pure integral-type PLL with a damping branch to enhance the stability of grid-tied inverter under weak grids," arXiv preprint arXiv:2401.02202, 2024. [Online]. Available: https://arxiv.org/pdf/2401.02202

[6] W. Du, Y. Liu, F. K. Tuffner, R. Huang, and Z. Huang, "Model specification of droop-controlled, grid-forming inverters (gfmdrp_a)," Pacific Northwest National Laboratory, Tech. Rep. PNNL-32278, 2021. [Online]. Available: https://www.pnnl.gov/main/publications/external/technical_reports/PNNL-32278.pdf

[7] D. Oliveira, G. C. B. Leal, D. Herrera, E. Galván-Díez, J. M. Carrasco, and M. Aredes, "An analysis on the VSC-HVDC contribution for the static voltage stability margin and effective short circuit ratio enhancement in hybrid multi-infeed HVDC systems," *Energies*, vol. 16, no. 1, p. 532, 2023. [Online]. Available: https://psecommunity.org/wp-content/plugins/wpor/includes/file/2302/LAPSE-2023.6812-1v1.pdf

[8] Y. Yu, X. Zheng, H. Li, J. M. Guerrero, and A. Akhavan, "Coordinated control to achieve stability and dynamic response enhancement of weak-grid-connected inverters based on sequence-admittance models," *IET Renewable Power Generation*, vol. 16, no. 2, pp. 339–351, 2022.

[9] L. Ding, X. Lu, and J. Tan, "Small-signal stability analysis of low-inertia power grids with inverter-based resources and synchronous condensers," in *2022 IEEE Power & Energy Society Innovative Smart Grid Technologies Conference (ISGT)*. IEEE, 2022, pp. 1–5.

[10] J. S. Bryant, B. McGrath, L. Meegahapola, and P. Sokolowski, "Small-signal modeling and stability analysis of a droop-controlled grid-forming inverter," in *2022 IEEE Power & Energy Society General Meeting (PESGM)*. IEEE, 2022, pp. 1–5.

979-8-3315-8138-1